Christian Eberle, Peter Gerlinger, Klaus Peter Geigle, Manfred Aigner, Toward finite-rate chemistry large-eddy simulations of sooting swirl flames, Combustion Science and Technology 190 (2018) 1194-1217

The original publication is available at www.informaworld.com

https://doi.org/10.1080/00102202.2018.1443444

Or use open URL link
http://www.informaworld.com/openurl?genre=article&issn= 1563-521X &volume=190&issue=7&spage=1194;

Towards finite-rate chemistry large-eddy simulations of sooting swirl flames

Christian Eberle, Peter Gerlinger, Klaus Peter Geigle, Manfred Aigner*

Deutsches Zentrum für Luft- und Raumfahrt (DLR), Institut für Verbrennungstechnik, Stuttgart, Germany

Journal:
Combustion Science and Technology

* **Corresponding Author:**
Christian Eberle
Deutsches Zentrum für Luft-und Raumfahrt (DLR)
Institut für Verbrennungstechnik
Pfaffenwaldring 38-40
70569 Stuttgart
Germany
Phone: +49/711/6862-563
Fax: +49/711/6862-578
Email: christian.eberle@dlr.de

Other authors:
Prof. Peter Gerlinger
Universität Stuttgart

Dr. Klaus Peter Geigle
Deutsches Zentrum für Luft-und Raumfahrt (DLR)

Prof. Manfred Aigner
Deutsches Zentrum für Luft-und Raumfahrt (DLR)

Abstract

This paper presents time-resolved numerical simulations of a well-characterized sooting swirl flame at elevated pressure. Recently published unsteady Reynolds averaged Navier-Stokes simulations (URANS) are compared here to newly performed large eddy simulations (LES). Finite-rate chemistry, where transport equations are solved for each chemical species, is employed for the gas phase, a sectional approach for polycyclic aromatic hydrocarbons (PAHs), and a two-equation model for soot particles. Feedback effects such as the consumption of gaseous soot precursors by growth of soot and PAHs are inherently captured accurately by a coupled solution of the set of governing equations. The numerical results (velocity components, temperature and soot volume fraction) compare well with experimental data. No significant differences between URANS and LES are observed for time-averaged temperatures and velocity components, while the prediction of soot is significantly improved by LES. It will be shown that an accurate description of the instantaneous flame structure (especially of the hydroxyl radical distribution) by resolution of turbulent scales is of fundamental importance for accurate soot predictions in confined swirl flames with strong secondary air injection.

Keywords: Model combustor, Sooting swirl flame, Finite-rate chemistry, Unsteady Reynolds averaged Navier-Stokes simulation (URANS), Large eddy simulation (LES)

1 Introduction

Information about the soot evolution is of high relevance for the improvement of combustion devices. Soot has a high radiative emissivity and thereby contributes

significantly to locally elevated heat loads on combustion chamber walls (Nakamura et al., 1982). Knowledge of local soot concentrations may thus be important for the design of combustion chamber walls. Furthermore, the emission of particulate matter must be kept as low as possible due to the adverse effects of particulates on health, environment, and climate (Kärcher , ed.; Jensen and Toon, 1997; Petzold et al., 1998, 1999). This requires in-depth knowledge about soot formation and oxidation processes at technical combustion conditions. Soot predictions by means of CFD simulations are of high relevance in this context since they complement experimental investigations which in many cases are limited to exhaust gas analysis because optical access to the flame is not realizable. Previous soot CFD simulations of real scale aero-engine combustors (Blacha et al., 2011; Eberle et al., 2014; Lecocq et al., 2014; Mueller and Pitsch, 2013) lacked a rigorous model validation, because the experiments were limited to smoke number measurements at the combustor exit. So far detailed soot measurements were performed mainly for academic test cases like laminar flames (Arana et al., 2004; Figura and Gomez, 2014; Geigle et al., 2005; McEnally and Pfefferle, 2000; Saffaripour et al., 2011; Santoro et al., 1987; Tsurikov et al., 2005; Zhao et al., 2005) or turbulent jet flames (Gu et al., 2017; Köhler et al., 2012; Qamar et al., 2009). Such simple validation test cases are not representative for real scale devices, however. Therefore, Geigle et al. (2014; 2017; 2015a; 2015b) performed detailed measurements of a semi-technical model combustor. The ethylene fueled combustor provides well-defined boundary conditions and comprehensive validation data on one hand and on the other hand features technically relevant conditions such as a confined swirling flow and operation at elevated pressure. This combustor is a target case of the International Sooting Flame (ISF) workshop and has been in-

vestigated numerically by several authors. Koo et al. (2016) performed large-eddy simulations (LES) of an earlier version (Geigle et al., 2011) of the cited model combustor. Using a hybrid method of moments (HMOM) soot model (Mueller et al., 2009) and a radiation/flamelet progress variable (RFPV) combustion model (Ihme and Pitsch, 2008; Mueller and Pitsch, 2012), they obtained promising LES results. Using a similar modeling approach, Wick et al. (2017) obtained a good agreement to measured velocities and temperatures. Qualitatively, a reasonable agreement to the soot measurements was found. An overprediction of the maximum soot volume fraction was observed, however, and attributed to either the soot model itself or the combustion model which uses flamelet tables for non-premixed combustion. Dupoirieux et al. (2016) investigated the cited model combustor using LES with an artificially thickened flame (ATF) subgrid TCI model (Colin et al., 2000) and a two-equation soot model (Leung et al., 1991) and obtained a good quantitative agreement between LES results and measurements. Franzelli et al. (2015) used a similar modeling framework to compare a fully-tabulated chemistry model (Vicquelin et al., 2011) to a hybrid model (Lecocq et al., 2014) where a few species are transported to obtain the thermo-chemical state from look-up tables. Their LES results were encouraging, the peak soot volume fractions obtained by the two combustion models differed by about one order of magnitude, however. This indicates that the soot evolution in this combustor is sensitive to the type of combustion model used. That can be related to the complex combustion conditions encountered. In particular, partial premixing, mixing of recirculating burnt gas with fresh mixture, and the modeling of soot precursor consumption can be very challenging for tabulated chemistry approaches because their thermo-chemical manifold is limited by a priori generated look-up tables (Pope, 2013).

This clearly motivates the use of a more accurate description of combustion. In the present work this is obtained by using a finite-rate chemistry (FRC) model, which does not require a priori generated tables because combustion described by detailed reaction mechanisms is solved on the fly. Furthermore, FRC models allow a full coupling of soot and the thermo-chemical state of the gas phase by a simultaneous solution of all governing equations. Moreover, element conservation is ensured in this approach. The applicability of finite-rate chemistry for soot predictions in turbulent swirl flames was investigated by Eberle et al. (2015). Since LES-FRC simulations are computationally very expensive, especially at the high Reynolds numbers encountered in real-scale combustion devices (Gicquel et al., 2012), they decided to perform unsteady Reynolds averaged Navier-Stokes simulations (URANS). The applicability of URANS for such applications was demonstrated earlier by Bolla et al. (2014) who performed CFD soot simulations in a heavy-duty diesel engine.

The URANS results of Eberle et al. (2015) showed good agreement with measurements in terms of time-averaged velocity components and time-averaged temperature; also a precessing vortex core (PVC) was resolved in accordance with the experiments from Geigle et al. (2017). However, deviations between measured and calculated soot distributions were observed and partially attributed to the limitations of statistical turbulence modeling. In particular it was found that URANS, in contrast to the measurements of Geigle et al. (2015a), persistently predicted high hydroxyl (OH) concentrations on the center line of the combustor close to the stagnation point between the inner recirculation zone and the inflow. This prevented soot presence in this region because of the high oxidative potential of OH. For clarification of these earlier findings, LES of the model combustor are conducted

in this work, employing the DLR THETA code (Di Domenico, 2008) and a two equation soot model which has been used in a number of previous works (Blacha et al., 2011; Di Domenico et al., 2010; Eberle et al., 2014, 2015). The LES results will be compared to recently published URANS results (Eberle et al., 2015) and differences will be analyzed.

2 Methodology

Basis of this work are the soot and PAH models implemented in the DLR code THETA (Di Domenico et al., 2010; Blacha et al., 2012). THETA is an unstructured finite-volume solver which has been optimized for low Mach number combustion problems. Combustion is modeled by finite-rate chemistry. PAHs are described by a sectional approach where transport equations are solved for each section and soot is treated by a two equation model. Chemical reactions involving soot and PAHs are formulated in Arrhenius form and are solved in the same way as reactions of gas phase species. This allows a full coupling of soot, PAHs, and gas phase species. Feedback effects of soot and PAHs on the gas phase such as consumption of gaseous soot precursors (predominantly acetylene, benzene and toluene) as well as heat radiation are thus inherently captured accurately.

2.1 Governing Equations

The filtered and modeled equations for conservation of mass and momentum read

$$\frac{\partial \overline{\rho}}{\partial t} + \frac{\partial \overline{\rho}\widetilde{u}_i}{\partial x_i} = 0 \,, \tag{1}$$

$$\frac{\partial \overline{\rho}\widetilde{u}_i}{\partial t} + \frac{\partial \overline{\rho}\widetilde{u}_i\widetilde{u}_j}{\partial x_j} + \frac{\partial \overline{p^*}}{\partial x_i} - 2\frac{\partial}{\partial x_j}\left((\mu+\mu_t)\left(\widetilde{S}_{i,j} - \frac{1}{3}\widetilde{S}_{k,k}\delta_{i,j}\right)\right) = \overline{\rho} g_i \,. \tag{2}$$

The overbars $\overline{\phi}$ and $\widetilde{\phi}$ denote Reynolds and Favre averages in the URANS context and respective filtering operations in the LES context. u_i is the velocity component in x_i-direction, ρ the density, μ the molecular viscosity, μ_t the turbulent viscosity, $S_{i,j}$ the strain tensor, and g_i the gravity constant in x_i-direction. The pseudo-pressure p^* is defined as $p^* = p + \frac{2}{3}\rho k \delta_{ij}$, with p being the pressure, k the turbulent kinetic energy, and δ_{ij} the Kronecker delta. In case of URANS, μ_t is calculated by the two-equation shear stress transport (SST) turbulence model from Menter (1994) and in case of LES by the zero-equation wall adapting local eddy viscosity model (WALE) from Nicoud and Ducros (1999). The filtered and modeled transport equations of the specific enthalpy h (h is defined as the sum of thermal and chemical enthalpy) and reactive scalars Y_α (including mass fractions of gaseous and PAH species, soot mass fraction Y_s, and soot particle number density n_s) read

$$\frac{\partial \overline{\rho}\widetilde{h}}{\partial t} + \frac{\partial \overline{\rho}\widetilde{u}_i\widetilde{h}}{\partial x_i} - \frac{\partial}{\partial x_i}\left(\left(\frac{\lambda}{c_p} + \frac{\mu_t}{\mathrm{Pr}_t}\right)\frac{\partial \widetilde{h}}{\partial x_i}\right) = \overline{\omega}_h \,, \tag{3}$$

$$\frac{\partial \overline{\rho}\widetilde{Y}_\alpha}{\partial t} + \frac{\partial \overline{\rho}\widetilde{u}_i\widetilde{Y}_\alpha}{\partial x_i} - \frac{\partial}{\partial x_i}\left(\left(\frac{\mu}{\mathrm{Sc}} + \frac{\mu_t}{\mathrm{Sc}_t}\right)\frac{\partial \widetilde{Y}_\alpha}{\partial x_i}\right) = \overline{\omega}_\alpha \,, \tag{4}$$

where λ is the thermal conductivity, c_p the specific heat at constant pressure, Pr_t = 0.7 the turbulent Prandtl number, and Sc and Sc_t = 0.7 the laminar and turbulent Schmidt number, respectively. Due to the large Schmidt number of soot particles ($1/\mathrm{Sc} \to 0$), molecular diffusion is neglected for Y_s and n_s, while $\mathrm{Sc} = 0.7$ is chosen for other reactive scalars. The source terms ω_h and ω_α describe heat radiation and consumption as well as production of reactive species due to chemical reactions. Assuming an optically thin medium, the radiative heat loss is given by the Stefan-Boltzmann law

$$\omega_h = -4\ \sigma_S\ \varepsilon\ T^4\ , \tag{5}$$

with σ_S = 5.669 $\times$ 10^{-8} W m^{-2} K^{-4} being the Stefan-Boltzmann constant and ε the emissivity factor. To ensure comparability with previous results (Eberle et al., 2015), the radiation model from Di Domenico et al. (2010) which assumes radiative heat losses in confined ethylene flames to be dominated by soot radiation is used in this work as well. The emissivity factor is described as a function of temperature and soot volume fraction as

$$\varepsilon = 411\ T f_v\ . \tag{6}$$

The constant 411 was obtained by calibration using soot and PAH models which are very similar to those applied in the present work. This comparable simple and efficient model was further tested in later works (Blacha et al., 2012; Eberle et al., 2015) and generally led to satisfactory temperature predictions. The chemical

source term of a reactive scalar α reads

$$\omega_\alpha = M_\alpha \sum_{r=1}^{N_r} \left(\nu''_{\alpha,r} - \nu'_{\alpha,r}\right) \left\{ k_{f,r} \prod_{\beta=1}^{N_{sp}} C_\beta^{O'_{\beta,r}} - k_{b,r} \prod_{\beta=1}^{N_{sp}} C_\beta^{O''_{\beta,r}} \right\} . \tag{7}$$

where M_α is the molar mass and N_r the number of reactions. O_β and $C_\beta = \rho Y_\beta / M_\beta$ are the reaction order and the concentration of species β. k_f and k_b are forward and backward rate coefficients which are modeled by Arrhenius equations.

A major issue in turbulent combustion LES is the calculation of the filtered chemical source term $\overline{\omega_\alpha(T,Y)}$, which is a non-linear function of temperature and species mass fractions and thus involves unclosed correlations which are frequently referred to as subfilter turbulence chemistry interaction (TCI). Different closures for these subfilter TCI have been developed and some of them are reviewed in (Gicquel et al., 2012; Pitsch, 2006; Pope, 2013). These models differ significantly in complexity (and thus in computational cost) and even very detailed models feature modeling uncertainties. A simple subfilter model is the quasi laminar chemistry (QLC) approach (also referred to as implicit LES closure (Duwig et al., 2011; Hodzic et al., 2017)) where chemical source terms are evaluated directly on the filtered thermo-chemical variables

$$\overline{\omega_\alpha(T,Y)} = \omega_\alpha(\widetilde{T},\widetilde{Y}) \tag{8}$$

While this approach is not applicable to (U)RANS (Duwig et al., 2011), some authors report that it can be a reasonable approximation for LES if the flame is 'adequately' resolved (Duwig et al., 2011; Edwards et al., 2012; Fulton et al., 2016; Hodzic et al., 2017; Lourier et al., 2015; Potturi and Edwards, 2015; Ranjan

et al., 2016; Strakey and Eggenspieler, 2010; Zhang et al., 2015, 2010). Fulton et al. (2016) for example obtained reasonable LES-QLC results using an average mesh spacing which was half the laminar flame thickness. Another example is the LES-QLC simulation of Strakey and Eggenspieler (2010) which showed a good agreement to OH-measurements and little differences compared to LES-ATF (Colin et al., 2000) and LES-EBU (eddy-break-up model) (Spalding, 1971) simulations. This good performance has been attributed to a relatively fine grid.

The subfilter dynamics of the soot aerosol require a special consideration since soot structures are highly intermittent in space and time. Also, due to the high Schmidt number of soot particles, soot dynamics are characterized by very small Batchelor scales (Paul et al., 2004). In other words, they can occur at very small length scales, which in practice cannot be resolved by an LES grid. By assuming statistical independence of gas phase scalars and soot moments, Mueller and Pitsch (2011) developed a presumed PDF closure for the soot subfilter dynamics. In this model, the intermittent nature of these dynamics is accounted for by two δ-functions. Donde et al. (2013) proposed a soot subfilter model where stochastic transport equations are solved in a Lagrangian framework to obtain the joint PDF of gas phase scalars (mixture fraction, progress variable, and enthalpy) and soot moments. The influence of soot subfilter dynamics on the resolved statistics of soot evolution was not quantified, however. Other examples where subfilter TCI models for gaseous combustion were extended to describe the subfilter dynamics of the solid phase are the linear eddy model (LEM) (El-Asrag and Menon, 2009) and conditional moment closure (CMC) (Bolla et al., 2014; Kronenburg et al., 2000). Such approaches, however, are computationally very expensive especially when coupled to finite-rate chemistry models with detailed mechanisms.

There are on the other hand several recent turbulent flame simulations where promising results have been obtained without an explicit modeling of the soot subfilter dynamics (Dupoirieux et al., 2016; Hessel et al., 2014; Lecocq et al., 2014; Shahriari et al., 1995). This seems to indicate some robustness with respect to soot subfilter dynamics at least as far as resolved bulk soot properties such as soot volume fractions are concerned. In this work, it was therefore deliberately decided to take the QLC assumption for subfilter TCI and subfilter soot dynamics. For reasons of consistency, the radiation term is also evaluated directly on the filtered variables $\overline{\omega_h}(T, f_v) = \omega_h(\widetilde{T}, \widetilde{f_v})$. As we consider subfilter modeling to be important for more detailed investigations, the present QLC-LES simulation and our experience in TCI modeling (Fiolitakis et al., 2014; Gerlinger, 2003, 2017; Gerlinger et al., 2001, 2005) will serve as a starting point for future works which will address the treatment of soot subfilter dynamics.

2.2 Gas Phase Chemistry

The kinetics of gas phase species are modeled by a reaction mechanism which describes the formation of aromatic hydrocarbons up to benzene and toluene and has been validated for the combustion of small hydrocarbons, such as methane or ethylene at atmospheric and high-pressure conditions (Slavinskaya and Frank, 2009; Slavinskaya and Haidn, 2008). The mechanism includes 43 species and 304 elementary reactions.

2.3 PAH Model

PAHs are modeled by a sectional approach, where aromatic species with a molar weight between 100 and 800 g/mol are discretized by three logarithmically scaled

sections. PAH chemistry is divided into four sub mechanisms: PAH formation, C_2H_2 addition, PAH collisions, and PAH oxidation. As the PAH model is described in detail by Blacha et al. (2012), only a brief overview is given here. PAH formation, or rather interaction between gas phase and PAH_0 in general, is modeled by 19 reversible reactions derived from the detailed reaction mechanisms of Richter et al. (2005) and Slavinskaya and Frank (2009). An example is the reaction $C_7H_7 + CH_2 = A1C_2H_3 + H$, where styrene is replaced by (ν PAH0) and the stoichiometric coefficient ν is calculated from the conservation of mass. A full list of reactions and reaction rate parameters is given by Blacha et al. (2012). PAH growth is described by the HACA (hydrogen abstraction - acetylene addition) mechanism from Frenklach and Wang (1994) and by PAH collisions,

$$\mathrm{PAH}_k + \mathrm{PAH}_j \rightarrow \nu_1'' \ \mathrm{PAH}_k + \nu_2'' \ \mathrm{PAH}_{k+1} + \nu_{\mathrm{H_2}}'' \mathrm{H_2}, \tag{9}$$

with $j \leq k$, where for $k = 3$, PAH_{k+1} is replaced by soot. In this way, PAH growth reactions which involve the last PAH bin as reactant describe soot inception. The rate of reaction (9) is determined by the kinetic theory of gases using a constant collision efficiency $\gamma_{k,j} = 0.3$. Following Pope and Howard (1997) stoichiometric coefficients are calculated depending on intra sectional distribution functions and atom conservation. Regarding PAH oxidation, the two oxidants OH and O_2 are considered.

2.4 Soot Model

Different techniques for the statistical approximation of the soot particle size distribution (PSD) have been developed. In two-equation models, a monodisperse soot

PSD and spherical soot particles are assumed (Leung et al., 1991; Zamuner and Dupoirieux, 2000). A more detailed statistical approximation of the soot PSD is given by the method of moments (Donde et al., 2013; El-Asrag and Menon, 2009; Frenklach and Harris, 1987; Mueller and Pitsch, 2013), where transport equations for moments of the soot PSD are solved. In sectional approaches (Blacha et al., 2012; D'Anna and Kent, 2008; Dworkin et al., 2011; Lindstedt and Waldheim, 2013; Richter et al., 2005; Smooke et al., 2005), the soot PSD is discretized into sections with averaged chemical and physical properties. A detailed but costly description of the soot PSD is provided by Monte Carlo simulations (Morgan et al., 2007; Mosbach et al., 2009). Due to their computational efficiency two equation soot models are widely used for simulations of complex combustion configurations as for example turbulent jet flames (Kronenburg et al., 2000), gas turbine combustors (Lecocq et al., 2014) or diesel engines (Bolla et al., 2014). Therefore, a two equation model where the soot is described by the soot mass fraction Y_s and the soot particle number density n_s is used in the present work. This model considers soot surface growth by acetylene addition and PAH condensation, coagulation, and soot oxidation by OH and O_2. As discussed above, soot nucleation is described by PAH growth reactions which involve the last PAH section as reactant. A more detailed derivation is given by Blacha et al. (2011) and Di Domenico et al. (2010). The model is validated for laminar and turbulent combustion including different fuels ranging from methane to Jet-A1 surrogates. Using the same set of model constants for all simulations, a good overall agreement with experiments could be demonstrated (Blacha, 2012; Blacha et al., 2012; Köhler et al., 2012).

3 Results

3.1 Investigated Test Case

The set-up of the model combustor is illustrated in Fig. 1. The nozzle is fed by three concentric flows. Air at room temperature is injected through a central nozzle (diameter 12.3 mm) and an annular nozzle (inner diameter 14.4 mm, outer diameter 19.8 mm). Both air flows are fed from separate pleni and pass radial swirlers. Gaseous fuel (ethylene) is injected between the co-swirling air flows through 60 straight channels (0.5×0.4 mm^2). The fuel channels are resolved by the CFD grid and form a concentric ring mimicking the atomizing lip for spray combustion in aero-engine combustors (cf. Fig. 1(b)). The combustion chamber measures 120 mm in height and has a square cross section of 68×68 mm^2 with beveled edges. Four quartz windows (height 127 mm, width 59 mm) provide excellent optical access to the flame. Secondary air is injected from the four corners of the combustion chamber through ducts with 5 mm diameter at a height of 80 mm (cf. Fig. 1(a)). More details about burner configuration, test rig, and experimental setup are given by Geigle et al. (2014).

An operating point with a pressure of 3 bar and a thermal power of 38.6 kW is investigated. The equivalence ratio in the primary combustion zone is $\phi = 1.2$ and the total equivalence ratio including secondary air amounts to 0.86. The inflow boundary conditions are given in table 1. Comprehensive validation data obtained by laser diagnostics (velocity components by stereo-PIV (particle image velocimetry), temperatures by SV-CARS (shifted vibrational coherent anti-Stokes Raman scattering), soot volume fractions by LII (laser-induced incandescence), and PAH and OH concentrations by PLIF (planar laser-induced fluorescence)) is available

(Geigle et al., 2014, 2015a,b, 2017).

The simulations are performed on a three-dimensional tetrahedral grid with 6.6 million points corresponding to 36.5 million tetrahedra. The computational domain is shown in Fig. 1. The inflow boundaries are placed well upstream of the swirlers. Heat losses are taken into account by isothermal walls with estimated wall temperatures based on thermocouple measurements. These temperatures amount to 350 K for the swirlers, 600 to 700 K for the combustion chamber, and 900 K for the windows. The mesh was locally refined in the vicinity of the fuel channels to a spatial resolution of $\Delta x = \sqrt[3]{V_{\text{cell}}} \approx 0.05$ mm to properly resolve the mixing of fuel and air (cf. Fig. 1(b)). The resolution in the region of flame stabilization is 0.25 mm, while 0.5 mm are applied in the majority of the computational domain, and 1.0 mm towards the outlet passage. With this grid spacing the OH layer is resolved by 4 to 8 points in the region of flame stabilization and soot filaments are resolved by more than 5 points. The ratio of turbulent to molecular viscosity is frequently used to a posteriori evaluate the grid resolution. This ratio is significantly smaller than 10 in the present LES which indicates a good resolution of turbulent structures (Ivanova et al., 2012). Furthermore, the ratio of resolved to total temperature variance was evaluated and values greater than 0.9 suggest the subfilter variance of reactive scalars to be reasonably resolved (Lourier et al., 2015). Second order discretization schemes are used in space and time. A time step width of 0.5 μs was applied to ensure convergence. Pressure-velocity coupling is realized by a projection method from Chorin (1968). In total, 57 transport equations are solved (five equations for momentum, pressure correction and specific enthalpy; four equations for turbulence and TCI modeling (only in case of URANS); 43 equations for gas phase species; and five equations for PAHs and

soot, respectively). Statistics were sampled over a physical time of approximately 60 ms, which corresponds to about six flow through times based on bulk flow velocities and chamber length. One simulation took about 55 days on 256 cores ($\approx$ 338 000 CPU hours on Intel Xeon X5570 quad-core processors with a clock rate of 2.93 GHz).

3.2 Velocity Field

Figure 2 shows streamlines of representative calculated instantaneous flow fields. Dominant features of the turbulent swirling flame are the inner and outer recirculation zones (IRZ and ORZ) which provide heat and radicals for flame stabilization (Stöhr et al., 2015). Since statistically averaged equations are solved in URANS, the calculated velocity field displayed in Fig. 2(a) is per model definition periodic in time and smoother than the true turbulent field (Spalart, 2000). LES on the other hand resolves turbulent scales and thereby predicts significantly more complex flow patterns as shown in Fig. 2(b). In agreement to the measurements (Geigle et al., 2017; Boxx et al., 2016), both, URANS and LES predict a precessing vortex core (PVC). Spectra of axial velocity components at a probe point in the vicinity of the PVC (see the label in Fig. 2(a)) are given in Fig. 3. It has been shown by Eberle et al. (2015) that the velocity amplitudes at $f \approx 500$ Hz correspond to the hydrodynamic structure of the PVC. The predicted PVC frequencies ($f_{\mathrm{URANS}} = 515$ Hz, $f_{\mathrm{LES}} = 440$ Hz) agree well with experimental findings from Boxx et al. (2016).

Measured and predicted time-averaged axial velocities are compared in Fig. 4. The calculated velocity fields are very similar and agree well to the PIV-SoC (sum of correlation) data. The only notable difference between simulation and experiment is observed in the vicinity of the injection system, where the measured veloc-

ity peaks are wider then the predicted ones. This deviation has also been observed in the LES of Wick et al. (2017) and, as will be discussed in the following, can be attributed to the limitations of the SoC technique.

A comparison between simulation and experiment by means of radial profiles is given in the following. To this end, Figs. 5 to 7 show time-averaged and rms velocity components of the non-reacting flow field, while axial velocities at flame conditions are given in Fig. 8. Two experimental data sets are shown in the latter case. The statistical evaluation of PIV-FoV data (field of view) is more accurate than the PIV-SoC data (sum of correlation). While PIV-SoC provides only time-averaged velocities, more detailed information including instantaneous and rms velocities can be obtained by PIV-FoV (Geigle et al., 2017). Reliable PIV-FoV data could only be determined covering a small area of the flame due to the high complexity of the experimental setup (Geigle et al., 2017), however. Close to the burner (x = 4 mm and x = 12 mm), the flow field is characterized by velocity peaks and high rms values between inner and outer shear layer and by a pronounced IRZ. At x = 45 mm, the velocity distribution is more homogeneous and the central velocity plateau which develops downstream of secondary air injection is captured well by both, LES and URANS. At non-reacting conditions, time-averaged and rms velocities are predicted with excellent agreement. The deviations in v_{rms} and w_{rms} at x = 4 mm can be explained by the limited spatial resolution of the PIV system (1.7×1.7 mm^2) (Geigle et al., 2017). It should also be noted that the statistical evaluation of PIV data close to walls is very challenging. This applies in particular to the out-of-plane velocity component w. At flame conditions, the profiles show a qualitatively similar behavior, the uncertainty in both numerical results and experimental data is higher, however. The uncertainty in the predicted velocity

profiles results from feedback effects of the flame on the velocity, while the high soot luminosity complicates the evaluation of experimental data. This leads to significant differences between PIV-SoC and PIV-FoV data especially at x = 12 mm where wider velocity peaks are obtained by PIV-SoC. At the cited axial position, the calculated velocity peaks are sharper compared to the experiment, leading to a wider IRZ. Also, the maximum negative axial velocity in the IRZ is higher than in the experiment, especially in case of URANS at x = 4 mm. Given the high complexity and the mentioned challenges of the test case, a reasonably good agreement between simulation and experiment can be reported. This level of agreement is comparable to previous LES of sooting swirl flames (Koo et al., 2016; Wick et al., 2017) and no major differences in terms of time-averaged axial velocity are found between URANS and LES. LES however provides a more detailed representation of the instantaneous flow field (cf. Fig. 2) and more comprehensive statistics such as rms values.

3.3 Temperature

Measured and calculated temperatures are compared in Fig. 9, where radial profiles at x = 1, 12, 45, and 95 mm are shown. Time-averages are given on the left and rms values on the right side. At the most upstream position, measurements and LES show cold gas in the IRZ, while recirculating hot gas is present in the ORZ. This is in contrast to the URANS results where hot gas is also found in the IRZ, which is related to the overpredicted negative axial velocity (cf. Fig. 8). As a further difference, URANS underpredicts the temperature in the ORZ. The rms peaks in the vicinity of the burner axis are not resolved by the measurements and indicate the occasional presence of hot gas. At x = 12 mm, hot gas penetrates

the IRZ and low temperatures are observed only between the inner and the outer shear layer, where high rms temperatures indicate strong fluctuations of the flame. URANS overpredicts the width of the central hot temperature plateau while the LES temperatures between the inner and outer shear layer are higher than in the experiment. Taking into account that accurate temperature predictions in the region of flame stabilization are highly challenging under such complex conditions, a reasonably good agreement between simulation and experiment is obtained, despite the cited deviations.

The homogeneous temperature profile and the comparably low rms values at x = 45 mm indicate a largely burnt mixture. The very good agreement at x = 45 mm and in the post-quench region (x = 95 mm) suggests that heat losses are also well described. Overall, the level of agreement represents the state of the art (Dupoirieux et al., 2016; Wick et al., 2017) and, again, no significant differences are observed between URANS and LES.

3.4 Soot evolution

Measured (Geigle et al., 2015a) and calculated soot volume fractions are shown in Fig. 10. As discussed in detail in the work of Eberle et al. (2015), some characteristic differences between experiment and simulation are observed. Firstly, the maximum soot volume fraction in the LES ($f_{v,max}$ = 0.64 ppm) and the URANS ($f_{v,max}$ = 0.47 ppm) is significantly higher than in the experiment ($f_{v,max}$ = 0.037 ppm). A possible reason for this deviation is the irreversible description of PAH chemistry which has been shown to cause a too strong soot nucleation rate possibly leading to an overprediction of f_v (Eberle et al., 2017). In this study, Eberle et al. (2017) investigated the influence of PAH chemistry on soot predictions for a num-

ber of generic combustion problems and found that it was not possible to correctly predict the soot morphology using irreversible PAH chemistry, in particular in case of partially premixed combustion. Performing a source term analysis with subsequent integration over the plane shown in Fig. 10 yields a total soot growth term of 0.01 kg/(m^3 s) with the contributions of nucleation, PAH-condensation, and C_2H_2-addition being 8.6 %, 9.4 % and 82.0 %. In comparison to the literature (Eberle et al., 2017; Xu et al., 1997; Kazakov et al., 1995; Balthasar and Frenklach, 2005; Eaves et al., 2012), the contribution of nucleation to total soot growth is very high which possibly indicates significant errors from the simplified treatment of PAH chemistry. Thus, future studies of this burner should use a more accurate PAH chemistry. Another difference between simulation and experiment is observed in the ORZ. While the ORZ is soot free in both simulations, the measurements show low soot concentrations in this region, which seem to result from an overlapping of the ORZ and soot filaments. The low measured soot volume fractions of 0.005 ppm and less in the ORZ, however, indicate that these overlapping events do not occur frequently. Furthermore, soot is oxidized too fast. In both simulations, soot is completely oxidized downstream of an axial position of approximately 70 to 75 mm. This is in contrast to the measurements where soot is observed as far as 110 mm downstream of fuel injection. Finally, in contrast to measurements, URANS does not predict soot on the axis of the combustion chamber close to the stagnation point between the IRZ and inflow, whereas LES does accurately predict the shape of the soot distribution in this region. In the following, this significant difference between URANS and LES will be discussed in more detail.

Figure 11 compares time-averaged mass fractions of predicted and measured (Geigle et al., 2015b) soot precursor species (PAH and acetylene). Recirculation zones

are visualized by $u = 0$ isolines and the state of scalar mixing by mixture fraction isolines at $\xi = 0.15$ and $\xi = 0.064$, where the latter value indicates a stoichiometric mixture. Overall, the PAH and acetylene distributions obtained by URANS are more localized than the LES predictions. The LES results agree better to the experimental data, where PAHs appear to be almost evenly distributed. The URANS peak mass fractions of C_2H_2 and PAH are about factor two higher compared to LES. Neither URANS nor LES predict significant amounts of soot precursors on the burner axis, which indicates that soot nucleation and soot growth processes mainly occur in fuel rich regions outside the IRZ. Soot structures may then be convected into the IRZ towards the burner axis as suggested by the high soot concentrations found on the axis (cf. Fig. 10). Comparing the $\xi = 0.15$ isolines shows that scalar mixing is on average more intense in LES, whereby parts of the IRZ are on average fuel rich in LES. This has important implications on the soot evolution as will be discussed later. Fig. 12 shows predicted and measured OH distributions along with soot isolines. The soot and OH measurements were conducted by simultaneous application of LII and OH-PLIF (Geigle et al., 2015a). The instantaneous URANS distributions are smoother than the measured ones and, as analyzed by Eberle et al. (2015), show high OH concentrations on the center line of the combustor at any given instant in time. Thereby, the presence of soot on the center line is prevented due to the oxidative potential of OH. This persistent prediction of OH in the cited region is attributed to the limitations of URANS, which does not resolve turbulent scales but only coherent transient motion. LES, on the other hand, more accurately describes the wrinkled flame structure by resolving turbulent scales and subsequently predicts, in agreement to the measurements from Geigle et al. (2015a), zones with low OH concentrations, which are filled with

soot, while an overlapping of soot and OH is minor at any given instant in time and space. In other words, the instantaneous realizations show a strong anti-correlation of OH and soot. Those low OH zones are fuel-rich and explain why LES predicts higher mixture fractions in the IRZ than URANS (cf. Fig. 11). The overlapping of time-averaged soot and OH distributions (see bottom row of Fig. 12) results from statistical evaluation and does not represent a physically realizable state. Concerning the time-averaged OH distribution, LES agrees well to the measurements, while the URANS distribution is more localized with a pronounced maximum in the IRZ. The OH peak mass fractions obtained with URANS are higher compared to LES.

4 Conclusions

URANS and LES of a sooting swirl flame at elevated pressure using finite-rate chemistry have been performed successfully. In accordance to experimental data, a PVC at $f \approx 500$ Hz was observed in both simulations. Given the high complexity of the test case, measured and predicted velocities and temperatures agree reasonably well. While no significant differences between URANS and LES are observed for time-averaged axial velocities and temperatures, the shape of the soot distribution is better predicted by LES, as high soot concentrations are found on the flame axis. This is one the one hand related to the more intense mixing in LES which yields locally fuel-rich conditions in the IRZ. On the other hand, it has been found that an accurate description of the instantaneous OH distribution is important. The LES results and the measurements indicate soot nucleation and soot growth to occur mainly in fuel rich regions outside the IRZ. As suggested by

the high soot concentrations on the axis, some soot structures may be convected towards the burner axis. These soot structures are enveloped by zones with high OH concentrations. An overlapping of soot and OH is minor at any given instant in time and space.

Acknowledgments

The authors thank G. Eckel and A. Fiolitakis for their contribution to this work and gratefully acknowledge the computing time granted by the John von Neumann Institute for Computing (NIC) and provided on the supercomputer JURECA at Jülich Supercomputing Centre (JSC). Part of this work was funded by the European Commission within the project Fuel Injector Research for Sustainable Transport (FIRST) under contract no. 265848.

References

Arana, C. P., Pontoni, M., Sen, S., Puri, I. K., 2004. Field measurements of soot volume fractions in laminar partially premixed coflow ethylene/air flames. Combustion and Flame 138, 362–372.

Balthasar, M., Frenklach, M., 2005. Detailed kinetic modeling of soot aggregate formation in laminar premixed flames. Combustion and Flame 140, 130–145.

Bilger, R. W., Stårner, S. H., Kee, R. J., 1990. On reduced mechanisms for methane-air combustion in nonpremixed flames. Combustion and Flame 80, 135–149.

Blacha, T., 2012. Effiziente Rußmodellierung in laminaren und turbulenten Flammen unterschiedlicher Brennstoffe. Ph.D. thesis, Institute of Combustion Technology for Aerospace Engineering, Universität Stuttgart.

Blacha, T., Di Domenico, M., Gerlinger, P., Aigner, M., 2012. Soot predictions in premixed and non-premixed laminar flames using a sectional approach for PAHs and soot. Combustion and Flame 159, 181–193.

Blacha, T., Di Domenico, M., Rachner, M., Gerlinger, P., Aigner, M., 2011. Modeling of soot and NO_x in a full scale turbine engine combustor with detailed chemistry. In: Proceedings of the ASME Turbo Expo 2011: Power for Land, Sea and Air. No. GT2011-45084.

Bolla, M., Farrace, D., Wright, Y. M., Boulouchos, K., 2014. Modelling of soot formation in a heavy-duty diesel engine with conditional moment closure. Fuel 117, 309–325.

Boxx, I. G., Geigle, K. P., Carter, D. C., Meier, W., 2016. Effects of air staging on the dynamics of an ethylene-fueled gas turbine model combustor at elevated pressure. In: 18th International Symposium on the Application of Laser and Imaging Techniques to Fluid Mechanics.

Chorin, A. J., 1968. Numerical solution of the Navier-Stokes equations. Mathematics of Computation 22, 745–762.

Colin, O., Ducros, F., Veynante, D., Poinsot, T., 2000. A thickened flame model for large eddy simulations of turbulent premixed combustion. Physics of Fluids 12, 1843–1863.

D'Anna, A., Kent, J. H., 2008. A model of particulate and species formation applied to laminar, nonpremixed flames for three aliphatic-hydrocarbon fuels. Combustion and Flame 152, 573–587.

Di Domenico, M., 2008. Numerical simulations of soot formation in turbulent flows. Ph.D. thesis, Institute of Combustion Technology for Aerospace Engineering Universität Stuttgart.

Di Domenico, M., Gerlinger, P., Aigner, M., 2010. Development and validation of a new soot formation model for gas turbine combustor simulations. Combustion and Flame 157, 246–258.

Donde, P., Raman, V., Mueller, M. E., Pitsch, H., 2013. LES/PDF based modeling of soot-turbulence interactions in turbulent flames. Proceedings of the Combustion Institute 34, 1183–1192.

Dupoirieux, F., Bertier, N., Guin, C., Geigle, K. P., Eberle, C., Gerlinger, P., 2016. Methodology for the numerical prediction of pollutant formation in gas turbine combustors and associated validation experiments. Aerospace Lab 11, 1–20.

Duwig, C., Nogenmyr, K.-J., Chan, C.-k., Dunn, M. J., 2011. Large eddy simulations of a piloted lean premix jet flame using finite-rate chemistry. Combustion Theory and Modelling 15, 537–568.

Dworkin, S. B., Zhang, Q., Thomson, M. J., Slavinskaya, N. A., Riedel, U., 2011. Application of an enhanced PAH growth model to soot formation in a laminar coflow ethylene/air diffusion flame. Combustion and Flame 158, 1682–1695.

Eaves, N. A., Veshkini, A., Riese, C., Zhang, Q., Dworkin, S. B., Thomson, M. J.,

2012. A numerical study of high pressure, laminar, sooting, ethane-air coflow diffusion flames. Combustion and Flame 159, 3179–3190.

Eberle, C., Blacha, T., Gerlinger, P., Aigner, M., 2014. Numerical simulations of soot and NO_x distributions in a full scale aero-engine combustor at two different flight altitudes. In: Proceedings of the 52nd AIAA Aerospace Sciences Meeting. No. AIAA 2014-0132.

Eberle, C., Gerlinger, P., Aigner, M., 2017. A sectional PAH model with reversible PAH chemistry for CFD soot simulations. Combustion and Flame 179, 63–73.

Eberle, C., Gerlinger, P., Geigle, K. P., Aigner, M., 2015. Numerical investigation of transient soot evolution processes in an aero-engine model combustor. Combustion Science and Technology 187, 1841–1866.

Edwards, J. R., Boles, J. A., Baurle, R. A., 2012. Large-eddy/Reynolds-averaged Navier-Stokes simulation of a supersonic reacting wall jet. Combustion and Flame 159, 1127–1138.

El-Asrag, H., Menon, S., 2009. Large eddy simulation of soot formation in a turbulent non-premixed jet flame. Combustion and Flame 156, 385–395.

Figura, L., Gomez, A., 2014. Structure of incipiently sooting ethylene-nitrogen counterflow diffusion flames at high pressures. Combustion and Flame 161, 1587–1603.

Fiolitakis, A., Ess, P. R., Gerlinger, P., Aigner, M., 2014. Modeling of heat transfer and differential diffusion in transported PDF methods. Combustion and Flame 161, 2107–2119.

Franzelli, B., Riber, E., Cuenot, B., Ihme, M., 2015. Numerical modeling of soot production in aero-engine combustors using large eddy simulations. In: Proceedings of the ASME Turbo Expo 2015: Power for Land, Sea and Air. No. GT2015-43630.

Frenklach, M., Harris, S. J., 1987. Aerosol dynamics modeling using the method of moments. Journal of Colloid and Interface Science 118, 252–261.

Frenklach, M., Wang, H., 1994. Detailed mechanism and modeling of soot particle formation. In: Bockhorn, H. (Ed.), Soot Formation in Combustion. Springer Verlag.

Fulton, J. A., Edwards, J. R., Cutler, A., McDaniel, J., Goyne, C., 2016. Turbulence/chemistry interactions in a ramp-stabilized supersonic hydrogen-air diffusion flame. Combustion and Flame 174, 152–165.

Geigle, K. P., Hadef, R., Meier, W., 2014. Soot formation and flame characterization of an aero-engine model combustor burning ethylene at elevated pressure. Journal of Engineering for Gas Turbines and Power 136, 021505.

Geigle, K. P., Hadef, R., Stöhr, M., Meier, W., 2017. Flow field characterization of pressurized sooting swirl flames and relation to soot distributions. Proceedings of the Combustion Institute 36, 3917–3924.

Geigle, K. P., Köhler, M., O'Loughlin, W., Meier, W., 2015a. Investigation of soot formation in pressurized swirl flames by laser measurements of temperature, flame structures and soot concentrations. Proceedings of the Combustion Institute 35, 3373–3380.

Geigle, K. P., O'Loughlin, W., Hadef, R., Meier, W., 2015b. Visualization of soot inception in turbulent pressurized flames by simultaneous measurement of laser-induced fluorescence of polycyclic aromatic hydrocarbons and laser-induced incandescence, and correlation to OH distributions. Applied Physics B 119, 717–730.

Geigle, K. P., Schneider-Kühnle, Y., Tsurikov, M. S., Hadef, R., Lückerath, R., Krüger, V., Stricker, W., Aigner, M., 2005. Investigation of laminar pressurized flames for soot model validation using SV-CARS and LII. Proceedings of the Combustion Institute 30, 1645–1653.

Geigle, K. P., Zerbs, J., Köhler, M., Stöhr, M., Meier, W., 2011. Experimental analysis of soot formation and oxidation in a gas turbine model combustor using laser diagnostics. Journal of Engineering for Gas Turbines and Power 133, 121503.

Gerlinger, P., 2003. Investigation of an assumed PDF approach for finite-rate chemistry. Combustion Science and Technology 175, 841–872.

Gerlinger, P., 2017. Lagrangian transported MDF methods for compressible high speed flows. Journal of Computational Physics 339, 68–95.

Gerlinger, P., Möbus, H., Brüggemann, D., 2001. An implicit multigrid method for turbulent combustion. Journal of Computational Physics 167, 247–276.

Gerlinger, P., Noll, B., Aigner, M., 2005. Assumed PDF modeling and PDF structure investigation using finite-rate chemistry. Progress in Computational Fluid Dynamics 5, 334–344.

Gicquel, L. Y. M., Staffelbach, G., Poinsot, T., 2012. Large eddy simulation of gaseous flames in gas turbine combustion chambers. Progress in Energy and Combustion Science 38, 782–817.

Gu, D., Sun, Z., Dally, B. B., Medwell, P. R., Alwahabi, Z. T., Nathan, G. J., 2017. Simultaneous measurements of gas temperature, soot volume fraction and primary particle diameter in a sooting lifted turbulent ethylene/air non-premixed flame. Combustion and Flame 179, 33–50.

Hessel, R., Reitz, R., Musculus, M., O'Connor, J., Flowers, D., 2014. A CFD study of post injection influences on soot formation and oxidation under diesel-like operating conditions. SAE International Journal of Engines 7, 694–713.

Hodzic, E., Alenius, E., Duwig, C., Szasz, R. S., Fuchs, L., 2017. A large eddy simulation study of bluff body flame dynamics approaching blow-off. Combustion Science and Technology 189, 1107–1137.

Ihme, M., Pitsch, H., 2008. Modeling of radiation and nitric oxide formation in turbulent nonpremixed flames using a flamelet/progress variable formulation. Physics of Fluids 20, 055110.

Ivanova, E., Noll, B., Griebel, P., Aigner, M., Syed, K., 2012. Numerical simulations of turbulent mixing and autoignition of hydrogen fuel at reheat combustor operating conditions. Journal of Engineering for Gas Turbines and Power 134, 041504.

Jensen, E. J., Toon, O. B., 1997. The potential impact of soot particles from aircraft exhaust on cirrus clouds. Geophysical Research Letters 24, 249–252.

Kärcher (ed.), B., 2008. Particles and cirrus clouds. Tech. rep., German Aerospace Center.

Kazakov, A., Wang, H., Frenklach, M., 1995. Detailed modeling of soot formation in laminar premixed ethylene flames at a pressure of 10 bar. Combustion and Flame 100, 111–120.

Köhler, M., Geigle, K. P., Blacha, T., Gerlinger, P., Meier, W., 2012. Experimental characterization and numerical simulation of a sooting lifted turbulent jet diffusion flame. Combustion and Flame 159, 2620–2635.

Koo, H., Hassanaly, M., Raman, V., Mueller, M. E., Geigle, K. P., 2016. Large-eddy simulation of soot formation in a model gas turbine combustor. Journal of Engineering for Gas Turbines and Power 139, 031503.

Kronenburg, A., Bilger, R. W., Kent, J. H., 2000. Modeling soot formation in turbulent methane air jet diffusion flames. Combustion and Flame 121, 24–40.

Lecocq, G., Poitou, D., Hernández, I., Duchaine, F., Riber, E., Cuenot, B., 2014. A methodology for soot prediciton including thermal radiation in complex industrial burners. Flow, Turbulence and Combustion 92, 947–970.

Leung, K. M., Lindstedt, R. P., Jones, W. P., 1991. A simplified reaction mechanism for soot formation in nonpremixed flames. Combustion and Flame 87, 289–305.

Lindstedt, R. P., Waldheim, B. B. O., 2013. Modeling of soot particle size distributions in premixed stagnation flow flames. Proceedings of the Combustion Institute 34, 1861–1868.

Lourier, M., Eberle, C., Noll, B., Aigner, M., 2015. Influence of turbulence-chemistry interaction modeling on the structure and the stability of a swirl-stabilized flame. In: Proceedings of the ASME Turbo Expo 2015: Power for Land, Sea and Air. No. GT2015-43174.

McEnally, C. S., Pfefferle, L. D., 2000. Experimental study of nonfuel hydrocarbons and soot in coflowing partially premixed ethylene air flames. Combustion and Flame 121, 575–592.

Menter, F. R., 1994. Two-equation eddy-viscosity turbulence models for engineering applications. AIAA Journal 32, 1598–1605.

Morgan, N., Kraft, M., Balthasar, M., Wong, D., Frenklach, M., Mitchell, P., 2007. Numerical simulations of soot aggregation in premixed laminar flames. Proceedings of the Combustion Institute 31, 693–700.

Mosbach, S., Celnik, M. S., Raj, A., Kraft, M., Zhang, H. R., Kubo, S., Kim, K., 2009. Towards a detailed soot model for internal combustion engines. Combustion and Flame 156, 1156–1165.

Mueller, M. E., Blanquart, G., Pitsch, H., 2009. Hybrid method of moments for modeling soot formation and growth. Combustion and Flame 156, 1143–1155.

Mueller, M. E., Pitsch, H., 2011. Large eddy simulation subfilter modeling of soot-turbulence interactions. Physics of Fluids 23, 115104.

Mueller, M. E., Pitsch, H., 2012. LES model for sooting turbulent nonpremixed flames. Combustion and Flame 159, 2166–2180.

Mueller, M. E., Pitsch, H., 2013. Large eddy simulation of soot evolution in an aircraft combustor. Physics of Fluids 25, 110812.

Nakamura, M., Koda, S., Akita, K., 1982. Sooting behavior and radiation in methanol/benzene/air diffusion flames. Proceedings of the Combustion Institute 19, 1395–1401.

Nicoud, F., Ducros, F., 1999. Subgrid-scale stress modelling based on the square of the velocity gradient tensor. Flow, Turbulence and Combustion 62, 183–200.

Paul, E. L., Atiemo-Obeng, V. A., Kresta, S. M., 2004. Handbook of Industrial Mixing: Science and Practice. John Wiley & Sons.

Petzold, A., Ström, J., Ohlsson, S., Schröder, F. P., 1998. Elemental composition and morphology of ice-crystal residual particles in cirrus clouds and contrails. Atmospheric Research 49, 21–34.

Petzold, A., Ström, J., Schröder, F. P., Kärcher, B., 1999. Carbonaceous aerosol in jet engine exhaust: emission characteristics and implications for heterogeneous chemical reactions. Atmospheric Environment 33, 2689–2698.

Pitsch, H., 2006. Large-eddy simulation of turbulent combustion. The Annual Reviews of Fuid Mechanics 38, 453–4582.

Pope, C. J., Howard, J. B., 1997. Simultaneous particle and molecule modeling (SPAMM): An approach for combining sectional aerosol equations and elementary gas-phase reactions. Aerosol Science and Technology 27, 73–94.

Pope, S. B., 2013. Small scales, many species and the manifold challenges of turbulent combustion. Proceedings of the Combustion Institute 34, 1–31.

Potturi, A. S., Edwards, J. R., 2015. Large-eddy/Reynolds averaged Navier-Stokes simulation of cavity-stabilized ethylene combustion. Combustion and Flame 162, 1176–1192.

Qamar, N. H., Alwahabi, Z. T., Chan, Q. N., Nathan, G. J., Roekaerts, D., King, K. D., 2009. Soot volume fraction in a piloted turbulent jet non-premixed flame of natural gas. Combustion and Flame 156, 1339–1347.

Ranjan, R., Muralidharan, B., Nagaoka, Y., Menon, S., 2016. Subgrid-scale modeling of reaction-diffusion and scalar transport in turbulent premixed flames. Combustion Science and Technology 188, 1496–1537.

Richter, H., Granata, S., Green, W. H., Howard, J. B., 2005. Detailed modeling of PAH and soot formation in a laminar premixed benzene/oxygen/argon low-pressure flame. Proceedings of the Combustion Institute 30, 1397–1405.

Saffaripour, M., Zabeti, P., Dworkin, S. B., Zhang, Q., Guo, H., Liu, F., Smallwood, G. J., Thomson, M. J., 2011. A numerical and experimental study of a laminar sooting coflow Jet-A1 diffusion flame. Proceedings of the Combustion Institute 33, 601–608.

Santoro, R. J., Yeh, T. T., Horvath, J. J., Semerjian, H. G., 1987. The transport and growth of soot particles in laminar diffusion flames. Combustion Science and Technology 53, 89–115.

Shahriari, B., Thomson, M. J., S., D., 1995. Development and validation of a partially coupled soot model for turbulent kerosene combustion in view of application to gas turbines. In: Proceedings of the ASME Turbo Expo 2015. No. GT2015-43063.

Slavinskaya, N. A., Frank, P., 2009. A modelling study of aromatic soot precursors formation in laminar methane and ethene flames. Combustion and Flame 156, 1705–1722.

Slavinskaya, N. A., Haidn, O. J., 2008. Reduced chemical model for high pressure methane combustion with PAH formation. In: Proceedings of the 46th AIAA Aerospace Sciences Meeting. No. AIAA 2008-1012.

Smooke, M. D., Long, M. B., Connelly, B. C., Colket, M. B., Hall, R. J., 2005. Soot formation in laminar diffusion flames. Combustion and Flame 143, 613–628.

Spalart, P. R., 2000. Strategies for turbulence modelling and simulations. International Journal of Heat and Fluid Flow 21, 252–263.

Spalding, D. B., 1971. Mixing and chemical reaction in steady confined turbulent flames. Proceedings of the Combustion Institute 13, 649–657.

Stöhr, M., Arndt, C. M., Meier, W., 2015. Transient effects of fuel-air mixing in a partially-premixed turbulent swirl flame. Proceedings of the Combustion Institute 35, 3327–3335.

Strakey, P. A., Eggenspieler, G., 2010. Development and validation of a thickened flame modeling approach for large eddy simulation of premixed combustion. Journal of Engineering for Gas Turbines and Power 132, 071501.

Tsurikov, M. S., Geigle, K. P., Krüger, V., Schneider-Kühnle, Y., Stricker, W., Lückerath, R., Hadef, R., Aigner, M., 2005. Laser-based investigation of soot formation in laminar premixed flames at atmospheric and elevated pressures. Combustion Science and Technology 177, 1835–1862.

Vicquelin, R., Fiorina, B., Payet, S., Darabiha, N., Gicquel, O., 2011. Coupling tabulated chemistry with compressible CFD solvers. Proceedings of the Combustion Institute 33, 1481–1488.

Wick, A., Priesack, F., Pitsch, H., 2017. Large-eddy simulation and detailed modeling of soot evolution in a model aero engine combustor. In: Proceedings of the ASME Turbo Expo 2017: Power for Land, Sea and Air. No. GT2017-63293.

Xu, F., Sunderland, P. B., Faeth, G. M., 1997. Soot formation in laminar premixed ethylene/air flames at atmospheric pressure. Combustion and Flame 108, 471–493.

Zamuner, B., Dupoirieux, F., 2000. Numerical simulation of soot formation in a turbulent flame with a Monte-Carlo PDF approach and detailed chemistry. Combustion Science and Technology 158, 407–438.

Zhang, L., Choi, J. Y., Yang, V., 2015. Supersonic combustion and flame stabilization of coflow ethylene and air with splitter plate. Journal of Propulsion and Power 31, 1242–1255.

Zhang, M., Hu, Z., Liu, P., 2010. Large-eddy simulation of kerosene spray combustion in a model scramjet chamber. Proceedings of the Institution of Mechanical Engineers Part G: Journal of Aerospace Engineering 224, 940–960.

Zhao, B., Yang, Z., Li, Z., Johnsten, M. V., Wang, H., 2005. Particle size distribution function of incipient soot in laminar premixed ethylene flames: effect of flame temperature. Proceedings of the Combustion Institute 30, 1441–1448.

Table 1: Operating point parameters. Reynolds numbers are based on the respective hydraulic diameter.

Inflow	mass flux [g/s]	Re/1000	T [K]
Ring air	7.08	15	293
Central air	3.03	17	293
Secondary air	4.04	14	293
Fuel C_2H_4	0.83	-	297

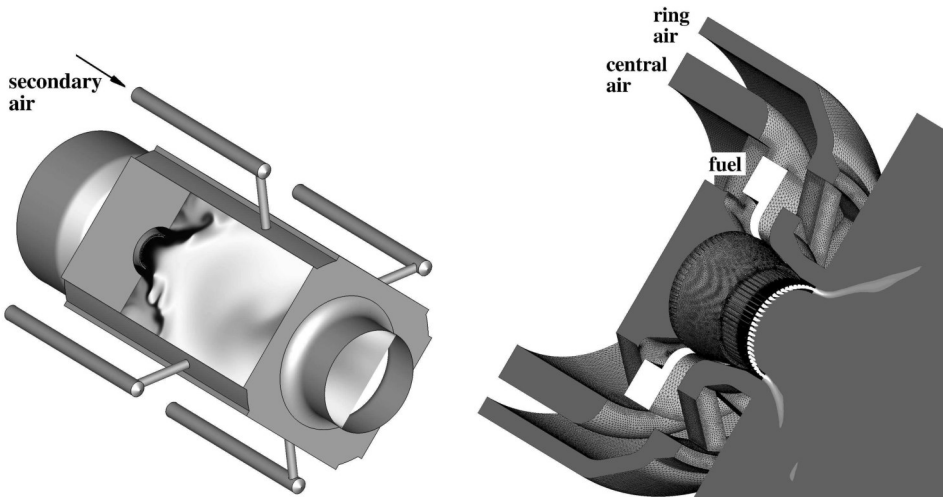

(a) Computational domain. (b) Injection system.

Figure 1: The model combustor. a) Computational domain with calculated temperature. b) Detailed view of the nozzle and the fuel injection system with calculated C_2H_4 mass fraction.

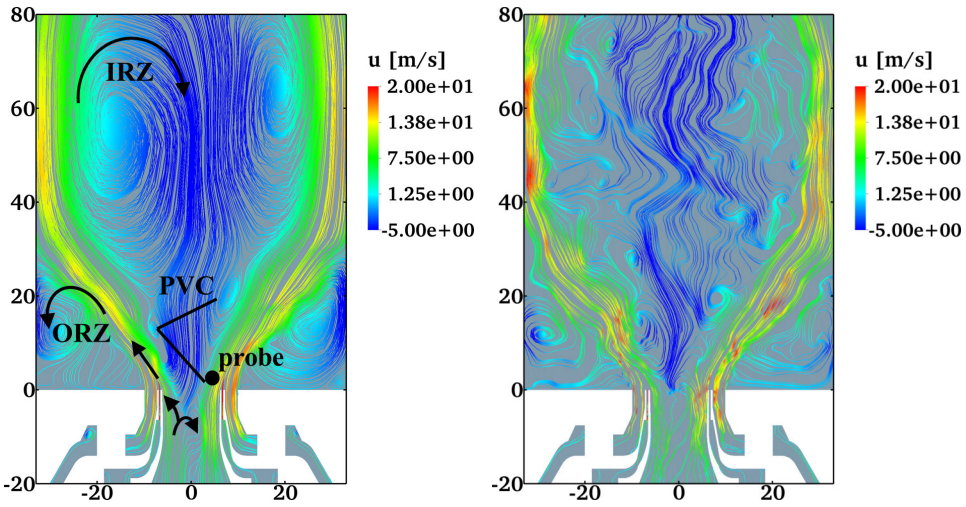

(a) URANS (b) LES

Figure 2: Streamline plots of representative calculated instantaneous flow fields. (a) URANS (b) LES. The dimensions are in mm and the color bar represents the axial velocity component. The probe point with r = 4 mm and x =3 mm is used later to obtain spectra.

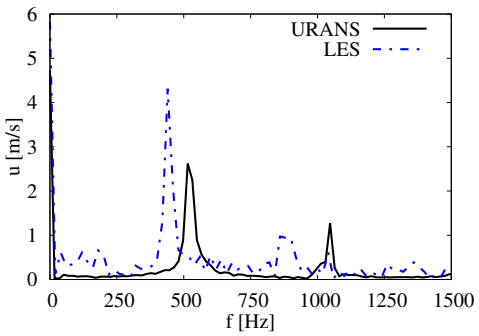

Figure 3: Spectra of the axial velocity component at the probe point labeled in Fig. 2(a).

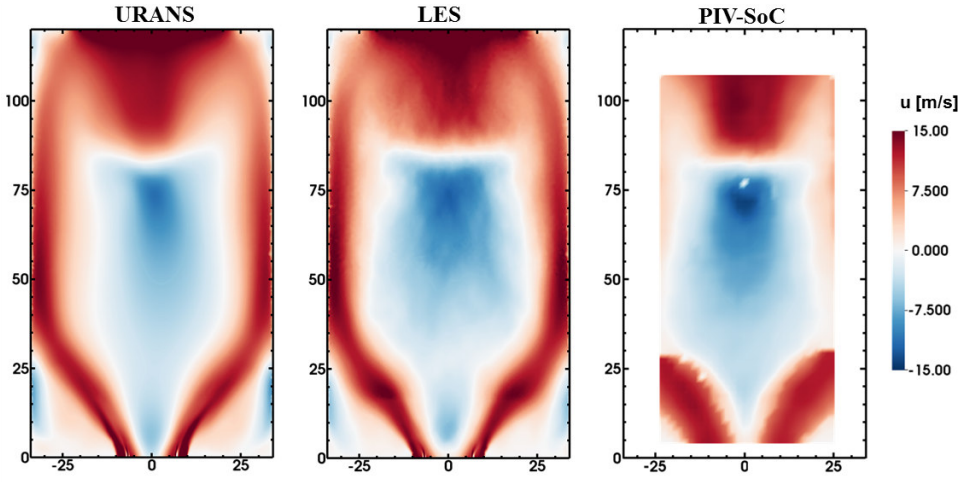

Figure 4: Predicted and measured (Geigle et al., 2017) time-averaged axial velocities. Dimensions are in mm.

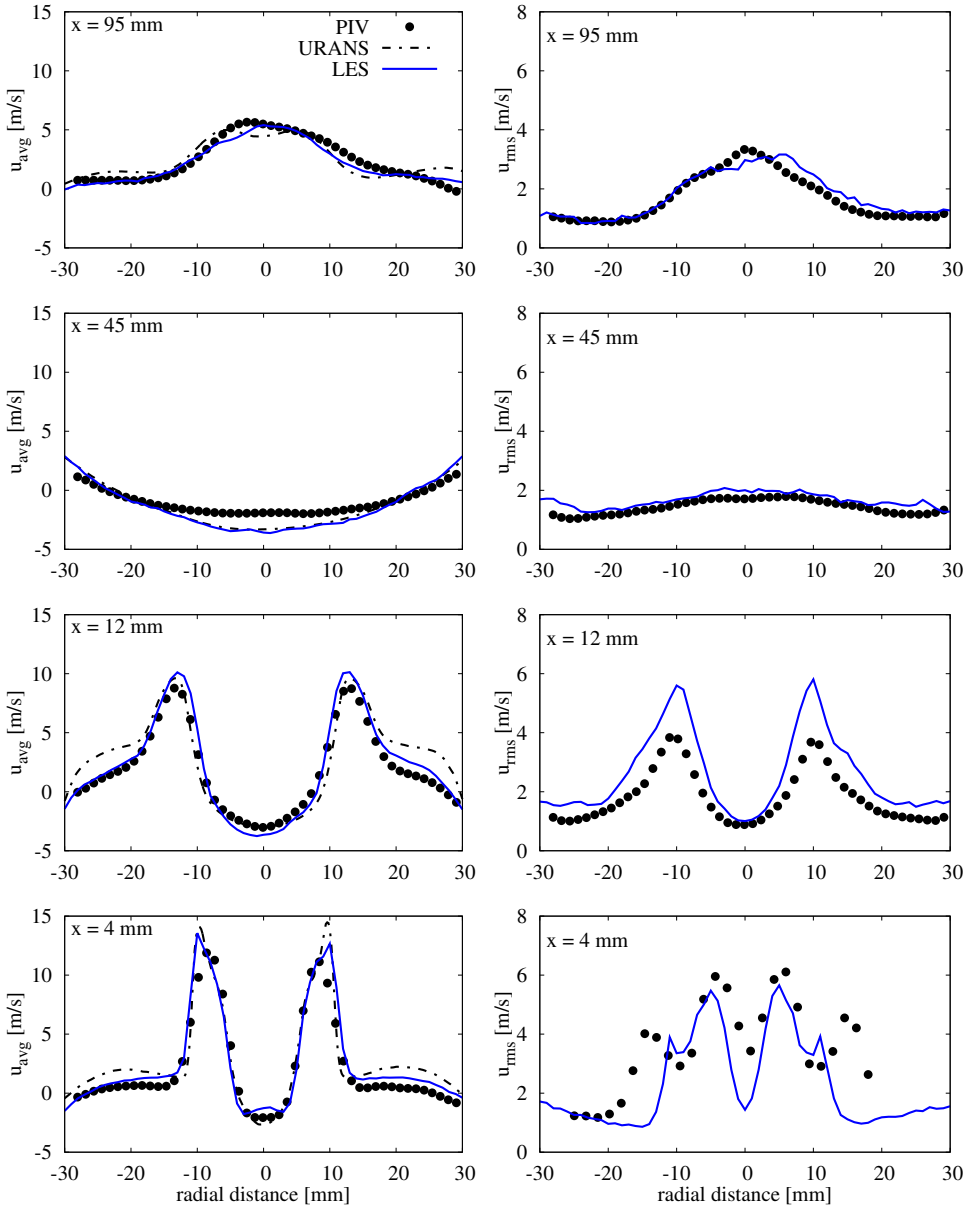

Figure 5: Radial profiles of predicted and measured (Geigle et al., 2017) axial velocities at non-reacting conditions. Time-averaged velocities are shown in the left column and rms velocities in the right column.

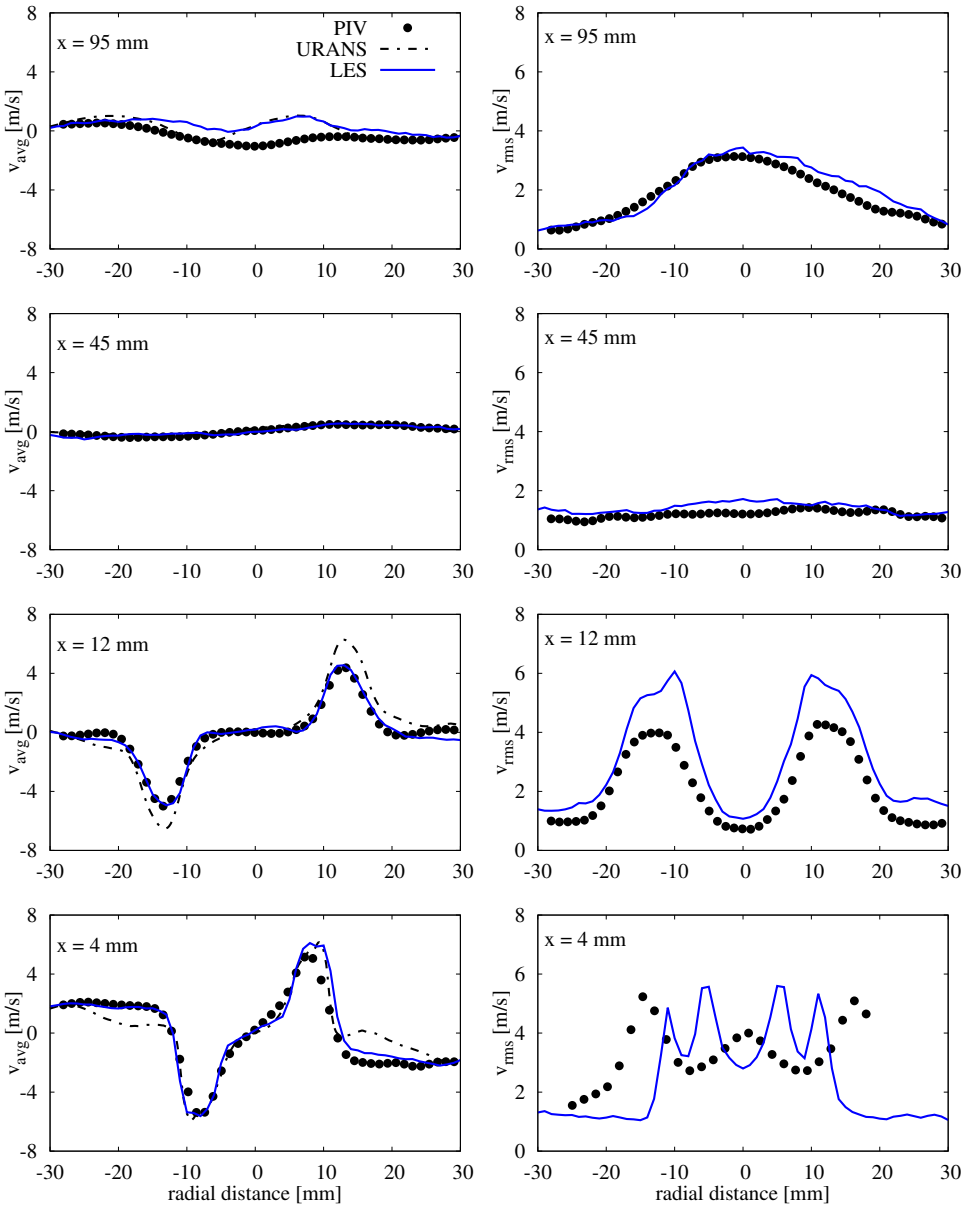

Figure 6: Radial profiles of predicted and measured (Geigle et al., 2017) radial velocities at non-reacting conditions. Time-averaged velocities are shown in the left column and rms velocities in the right column.

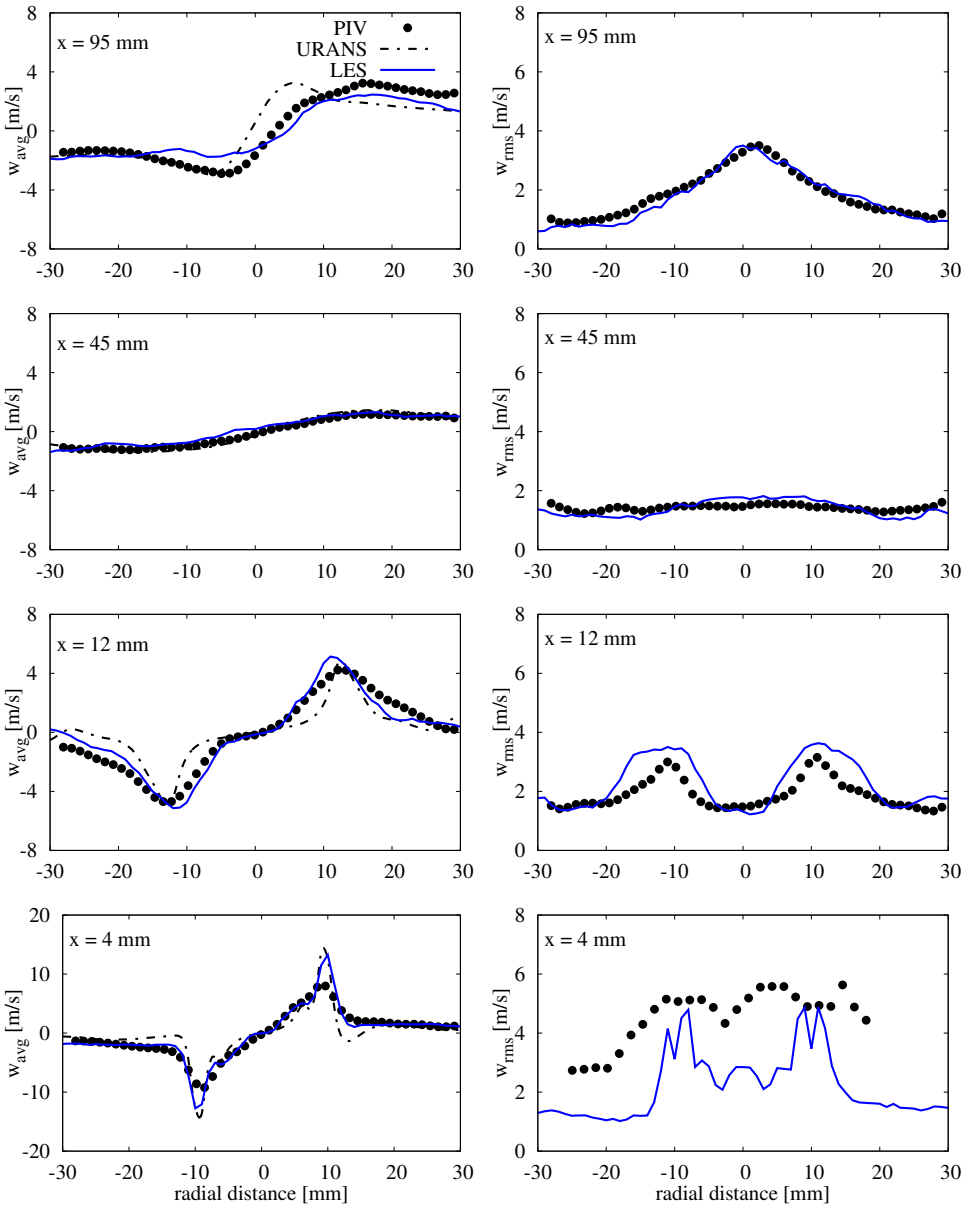

Figure 7: Radial profiles of predicted and measured (Geigle et al., 2017) tangential velocities at non-reacting conditions. Time-averaged velocities are shown in the left column and rms velocities in the right column.

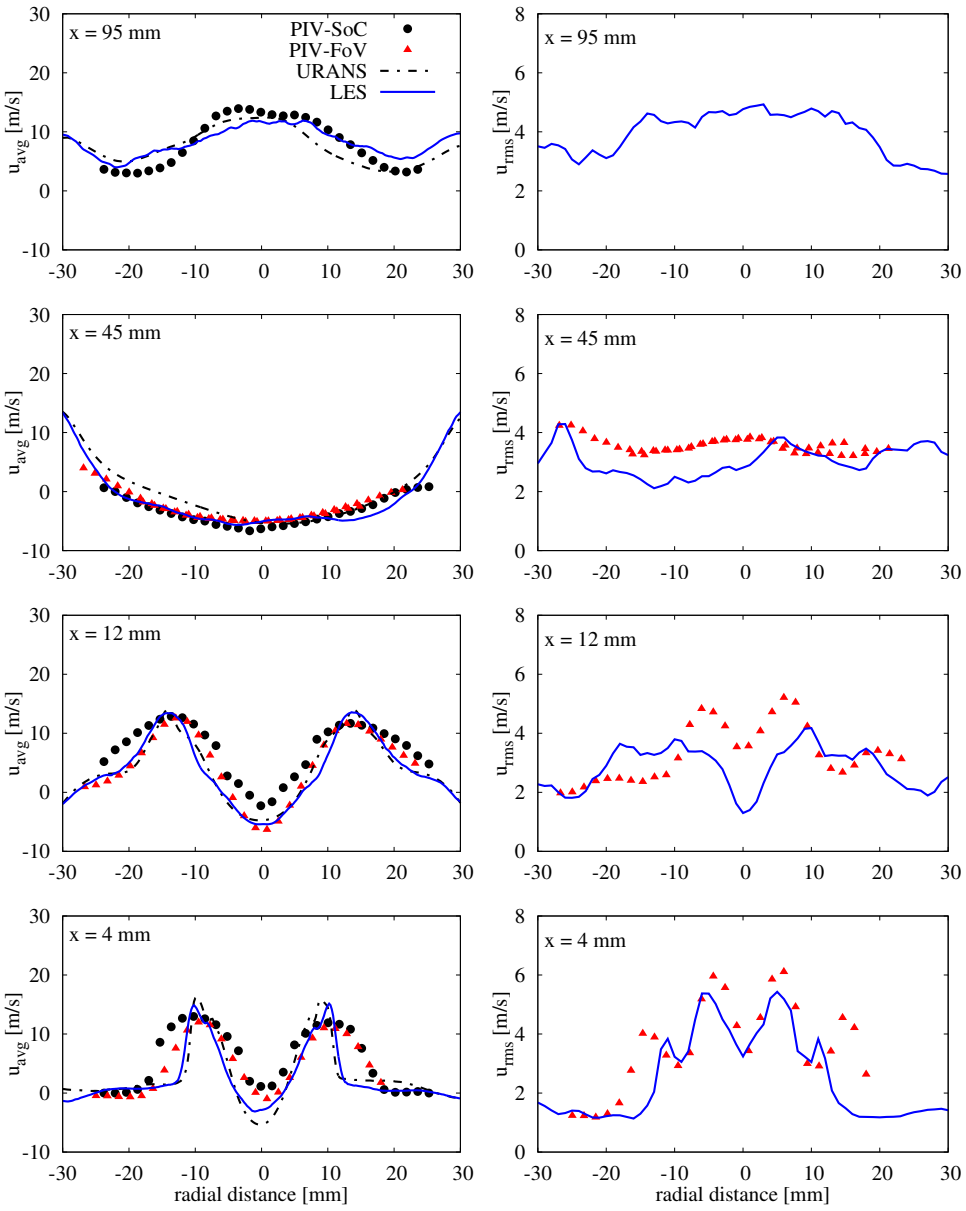

Figure 8: Radial profiles of predicted and measured (Geigle et al., 2017) axial velocities at reacting conditions. Time-averaged velocities are shown in the left column and rms velocities in the right column. Note that PIV-FoV data is not available at x = 95 mm and that PIV-FoV does not provide rms values.

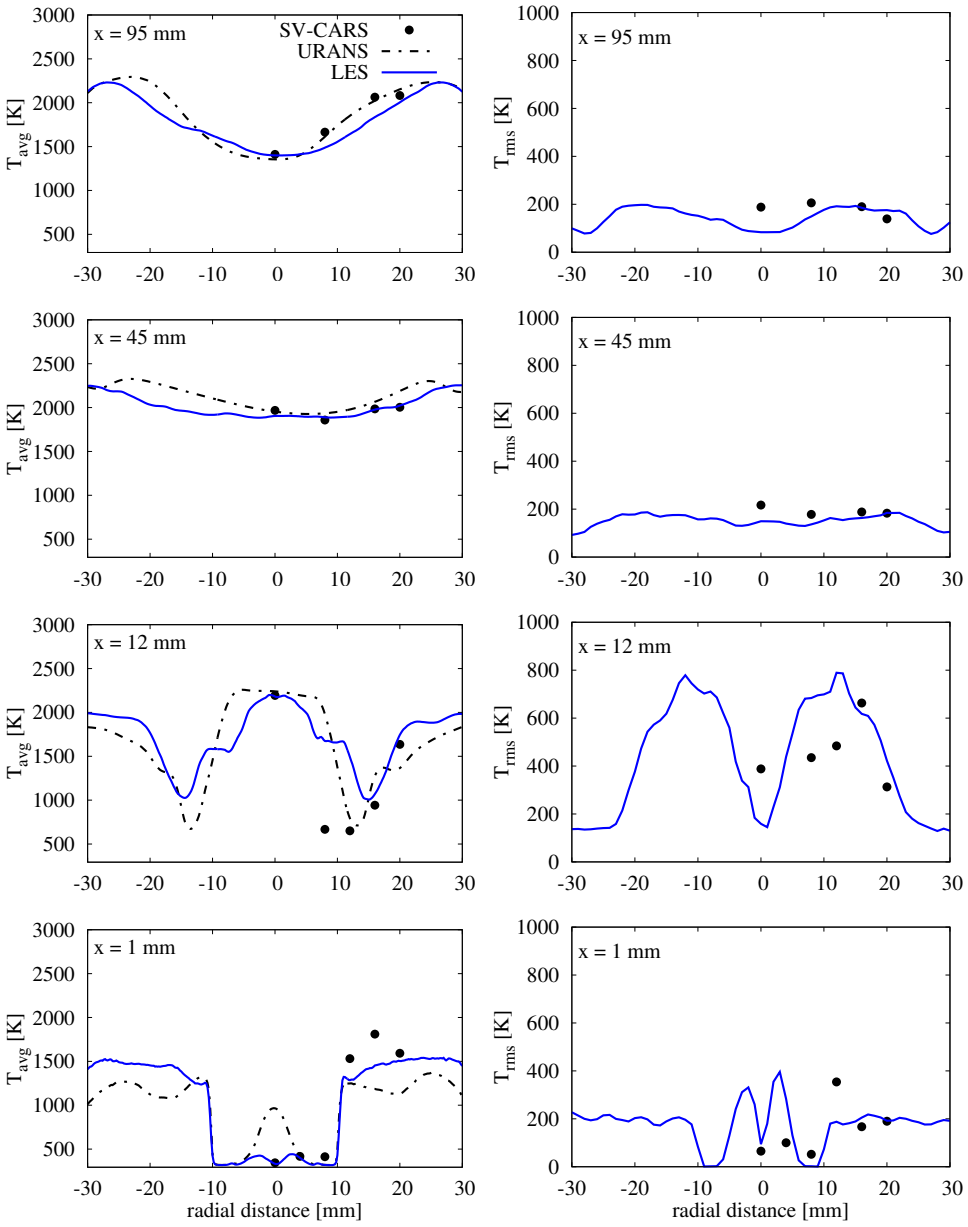

Figure 9: Radial profiles of predicted and measured (Geigle et al., 2015a) temperatures at selected downstream positions. Time-averaged temperatures are shown in the left column and rms temperatures in the right column.

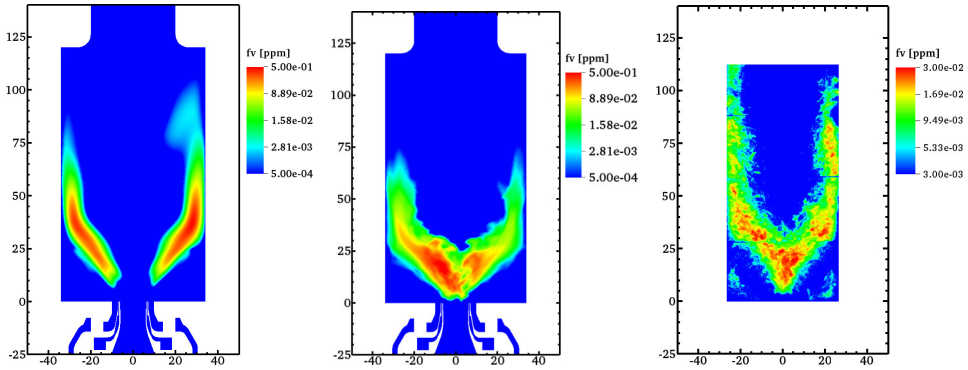

(a) URANS (b) LES (c) Experiment

Figure 10: Time-averaged soot volume fraction distributions: (a) Calculated f_v, URANS. (b) Calculated f_v, LES. (c) Measured f_v (Geigle et al., 2015a). A different color bar is used for the measurements. The dimensions are in mm.

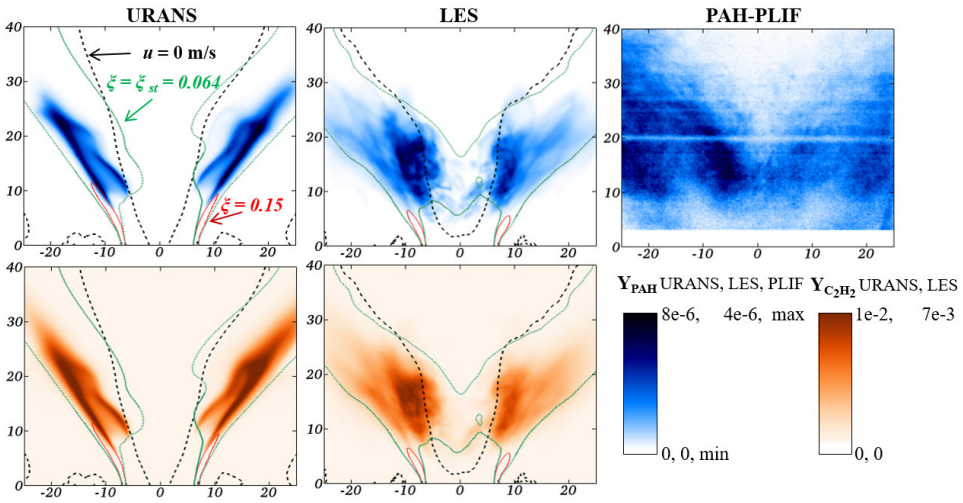

Figure 11: Time-averages of predicted and measured (Geigle et al., 2015b) PAH (top row) and acetylene (bottom row) mass fractions along with isolines of mixture fraction ξ and axial velocity u. The PAH-PLIF measurements are qualitative and the calculated PAH mass fraction is obtained by summation over all PAH bins ($Y_{\mathrm{PAH}} = \sum_i Y_{\mathrm{PAH}_i}$). The dimensions are in mm and ξ was calculated according to Bilger et al. (1990).

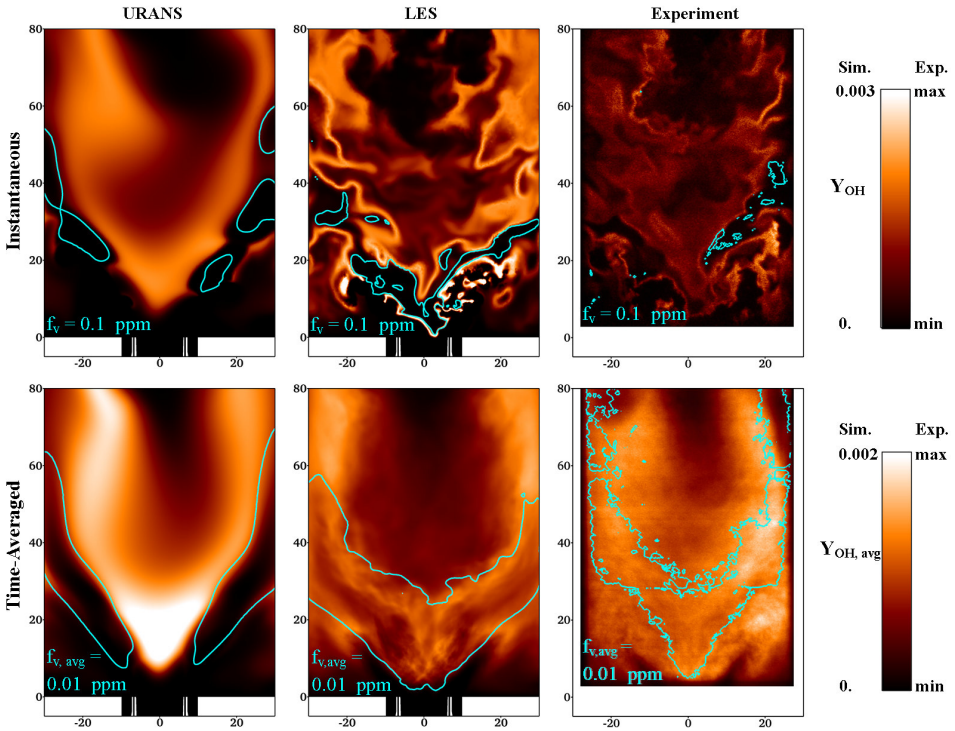

Figure 12: Predicted and measured (Geigle et al., 2015a) OH mass fractions with soot volume fraction isolines. Representative instantaneous realizations are shown in the top row and time-averages in the bottom row. Note that the OH-PLIF measurements are qualitative. Dimensions are in mm.